

Anisotropy of Langmuir turbulence and the Langmuir-enhanced mixed layer entrainment

Qing Li^{*} and Baylor Fox-Kemper*Department of Earth, Environmental and Planetary Sciences, Brown University,
Providence, Rhode Island 02912, USA*

(Received 3 August 2019; published 30 January 2020)

The anisotropy and structure of turbulence simulated by large-eddy simulations with and without Stokes-drift forcing are analyzed, with an emphasis on the linkage between the distinctive structure of Langmuir turbulence near the surface where cellular vortices aligned with the wind and wave propagation direction are apparent and the Langmuir-enhanced mixed layer entrainment at the base of the ocean surface boundary layer (OSBL) where turbulent structures differ. The tensor invariants of the Reynolds stresses, the variance of vertical velocity and buoyancy, and the velocity gradient statistics are used to categorize turbulence structures as a function of depth, including an extension of the barycentric map to show the direction as well as the magnitude of turbulence anisotropy and a vector-invariant extension of the Okubo-Weiss parameter. The extended anisotropic barycentric map and the velocity gradient statistics are demonstrated to be useful, providing compact information of the anisotropy, orientation, and structure of turbulent flows. It is found that the distinctive anisotropy and structures of Langmuir turbulence are quickly lost below regions where Stokes drift shear is significant and vortices are apparent, consistent with past observations and model results. As a result, the turbulent structures near the base of the OSBL are not significantly affected by the presence of Stokes drift above but are instead dominated by local Eulerian shear, except in one important manner. Langmuir turbulence does affect the mixed layer entrainment by providing extra available turbulent kinetic energy (TKE) via enhanced near-surface TKE production and higher vertical TKE transport energizing the turbulent structures near the base of the OSBL. The additional TKE is utilized by structures similar to those that exist without Stokes drift forcing in terms of anisotropy of their Reynolds stresses, but they are more energetic because of the Langmuir turbulence. Thus, parametrizing the major aspects of Langmuir turbulence on entrainment at the base of the OSBL can be incorporated through enhancing available energy without other modifications.

DOI: [10.1103/PhysRevFluids.5.013803](https://doi.org/10.1103/PhysRevFluids.5.013803)

I. INTRODUCTION

Shear turbulence and convective turbulence are two important types of turbulence that are commonly present in the planetary boundary layers and parameterized in various boundary layer turbulent closure schemes for geophysical fluid problems (e.g., Refs. [1–4]). Surface gravity waves at the free interface between the atmosphere and the ocean give rise to different types of turbulence—including wave breaking turbulence and Langmuir turbulence [5]. Langmuir turbulence results from interactions between the Stokes drift of ocean surface gravity waves [6–8] and

^{*}Present address: Fluid Dynamics and Solid Mechanics, Los Alamos National Laboratory, Los Alamos, NM 87545, USA; qingli@lanl.gov

Eulerian flows through the Stokes-vortex force [9], or equivalently Stokes shear force [10], and has distinctive structures than convective and shear turbulence [11,12]. Langmuir turbulence is the focus of this work, because it has been shown to be important in energizing the turbulent mixing throughout the ocean surface boundary layer (OSBL) and affecting the ocean mixed layer depth, thereby affecting the weather and climate through the air-sea exchange of heat, momentum, and tracers on a global scale [13–15].

Windrows commonly observed at the sea surface aligned with the wind and wave propagation are indicators of the presence of Langmuir turbulence. These windrows are debris agglomerations associated with parallel bands of convergent surface flows, with enhanced downward vertical velocity and downwind horizontal velocity located at the windrows, namely Langmuir circulation [16–18]. Such coherent circulation structures are responsible for the enhanced vertical velocity variance and vertical mixing as observed in a wavy OSBL compared with a wall-bounded layer, especially near the surface [14,19,20], although they are often found to be disordered—a condition called Langmuir turbulence [5]. These structures are frequently observed from bubble tracks and other methods detecting their strong vertical and cross-wind velocities (reviewed in Ref. [21]). These structures can also interact with the bottom boundary layer in a shallow coastal region and thereby affect the sediment transport [22]. As a practical observational and modeling alternative to mapping coherent structures within the complexity of Langmuir turbulence, sometimes Langmuir turbulence is taken to be any additional velocity variance or covariances beyond those expected from convective or shear forcing alone (e.g., Ref. [14]). Through this statistical approach, the authors have previously identified additional entrainment at the OSBL base due to Langmuir turbulence [23]. However, it is less clear what mechanisms Langmuir turbulence affects to enhance mixing and entrainment at the base of the OSBL—typically deeper than these coherent structures recognizably extend. Categorizing these mechanisms is the focus of this study.

In particular, direct observations of the three-dimensional (3D) flow in the open ocean show that distinctive structures of Langmuir circulation only appear within the upper half of a 40 to 60 m OSBL and find no direct effect of Langmuir circulation on the mixing near the base [24,25]. On the other hand, large-eddy simulations (LES) under similar conditions show enhanced vertical mixing at the base of the OSBL, thereby enhanced mixed layer entrainment, in the presence of Langmuir turbulence [5,23,26–28]. How can we reconcile the model results with the observations?

Langmuir turbulence derives additional energy from the Stokes drift of the ocean surface waves which decays exponentially or faster with depth (e.g., Ref. [29]), producing vanishingly small contributions below a few meters typically. Thus, there is usually no additional production of turbulent kinetic energy (TKE) due to Stokes drift near the base of the OSBL which is tens to hundreds of meters deep (e.g., Refs. [23,27]). The energy required by the Langmuir turbulence enhanced entrainment has to be from either the enhanced downward TKE transport or Stokes drift-modulated shear production at the base of the OSBL. Indeed, the deeply penetrating jets associated with the counterrotating Langmuir cells [30] may act as a media transporting TKE downward. On the other hand, enhanced shear instabilities beneath downwelling regions of Langmuir cells have been observed and are thought as mechanisms for thermocline erosion [31–33].

The above two mechanisms can each be predominant depending on the surface forcing regimes, e.g., (1) under weak to moderate wind conditions, downward TKE transport may dominate the energy source for the entrainment (e.g., the LES cases explored in Ref. [23]), and (2) under strong wind conditions, such as tropical cyclone conditions normally accompanied by strong inertial oscillation of the whole mixed layer, the local shear production near the base of the OSBL may be predominant (e.g., the LES cases explored in Ref. [34]). Note that while downward TKE transport sustains entrainment by providing necessary energy, entrainment reduces the local shear and thereby reduces the local shear production (increases the local Richardson number). Therefore, shear instability alone cannot sustain continuous entrainment without energy supply from above [35].

Focusing on the former regime, the authors [23] have shown that the effects of Langmuir turbulence on the entrainment can be represented by modifying the unresolved shear term in the

bulk Richardson number in the K-profile parameterization (KPP) [2], from which the OSBL depth is diagnosed. While a quantification of the Langmuir turbulence effects on modulating the shear instability near the base of the OSBL, and thereby on the entrainment, may require significant further work, this study aims at providing a clean description of the structure and anisotropy of Langmuir turbulence and their connections to the entrainment process at the OSBL base.

The structure and anisotropy of Langmuir turbulence have been studied in comparison with shear turbulence in LES studies (e.g., Refs. [5,11,27,36]), as well as using rapid-distortion theory [12,37,38]. However, none of them particularly discuss the structure of Langmuir turbulence at the base of the OSBL versus its signature structure near the surface and the implications for modeling the entrainment processes, which are the emphases of this study.

The remainder of this paper is structured as follows. The primary tool, a LES model is introduced in Sec. II. The structure and anisotropy of Langmuir turbulence simulated by LES, in comparison to shear turbulence, are explored in various ways in Sec. III. The linkage between these distinctive features of Langmuir turbulence and the entrainment at the base of the OSBL is discussed in Sec. IV. This paper ends with a brief discussion and main conclusions in Sec. V.

II. METHODS

A. Governing equations

The dynamics of Langmuir turbulence is governed by the wave-averaged Boussinesq equation (e.g., Refs. [9,17]), written in its Stokes shear force form [10],

$$\begin{aligned} \frac{\partial u_i}{\partial t} + u_j^L \frac{\partial u_i}{\partial x_j} &= -f \epsilon_{i3k} u_k^L - \frac{\partial p}{\partial x_i} - u_j^L \frac{\partial u_j^S}{\partial x_i} + b \delta_{i3} + \frac{\partial}{\partial x_j} (2\nu_t s_{ij}), \\ \frac{\partial u_i}{\partial x_i} &= 0, \\ \frac{\partial b}{\partial t} + u_j^L \frac{\partial b}{\partial x_j} &= \frac{\partial}{\partial x_j} \left(\kappa_t \frac{\partial b}{\partial x_j} \right), \end{aligned} \quad (1)$$

with $u_i^L = u_i + u_i^S$ the Lagrangian velocity, u_i^S the Stokes drift (constant in time), p the pressure divided by the reference density ρ_0 , b the buoyancy, ν_t the turbulent viscosity, s_{ij} the symmetric part of the velocity gradient tensor, κ_t the turbulent diffusivity, δ_{ij} the Kronecker delta, and ϵ_{ijk} the alternating tensor. Here the indices i, j , and k all take the values 1, 2, and 3, and summation over repeated indices is implied. All variables can be expressed as a sum of the mean and the perturbation using Reynolds decomposition, i.e., $v = \bar{v} + v'$ and $\overline{v'} = 0$. Here it is assumed that u_i^S is not affected by the turbulent flow and therefore is assumed to be known. In addition, $u_i^S = (u_1^S, u_2^S, 0)$ is assumed to be a function of only the depth, x_3 , so that if $(\bar{\quad})$ is taken as a temporal average or a horizontally spatial average, $\bar{u}_i^S = u_i^S$.

B. Large eddy simulation with Stokes forcing

Equations (1) are solved using large-eddy simulation technique [5,39] with a modified Smagorinsky [40] sub-grid-scale (SGS) scheme that solves a prognostic equation for SGS TKE [41]. The model and setup are essentially the same as Li and Fox-Kemper [23] and therefore only briefly described here. The simulation domain size is $L_i = (320, 320, 162.84)$ m, with $N_i = (256, 256, 256)$ computational cells in each direction, corresponding to a spatial resolution of $dx_i = (1.25, 1.25, 0.64)$ m. Integration time steps vary to satisfy the CFL condition (~ 3 s for nonrotating cases and ~ 6 s for rotating cases to be introduced below). All simulations are initialized from rest with small random perturbation in velocity near the surface to aid the development of turbulence. Initial stratification is neutral in the upper 42 m and stable below, where the Brunt-Väisälä frequency is $N = 6.2 \times 10^{-3} \text{ s}^{-1}$.

TABLE I. A summary of simulations. Acronyms in the name of simulations are as follows: ST, shear turbulence; LT, Langmuir turbulence; R, rotating; NR, nonrotating.

Simulations	f (s^{-1})	u_i^S	Description
ST-R	10^{-4}	0	w/o LT, weak shear at OSBL base
LT-R	10^{-4}	Eq. (2)	w/LT, weak shear at OSBL base
ST-NR	0	0	w/o LT, strong shear at OSBL base
LT-NR	0	Eq. (2)	w/LT, strong shear at OSBL base

Two pairs of simulations are conducted in this study. In each pair, simulations with Stokes forcing (denoted by a prefix *LT*) and without (denoted by a prefix *ST*) are conducted to highlight the effects of Langmuir turbulence. All four simulations are forced by identical surface stress, corresponding to a 10-m wind of $U_{10} = 5 \text{ m s}^{-1}$, and weak surface cooling of $Q_0 = 5 \text{ W m}^{-2}$ to promote the development of turbulence without significantly affecting the shear and Langmuir turbulence. The only difference between the two pairs is the Coriolis parameter, i.e., $f = 1.028 \times 10^{-4} \text{ s}^{-1}$ (corresponding to the value at 45°N) in one pair (denoted by a suffix *R*), whereas $f = 0$ in the other (denoted by a suffix *NR*). The mean horizontal velocity profiles in the former pair (ST-R and LT-R) exhibit Ekman spiral structure due to the rotation, and therefore a quasiequilibrium with the surface forcing is possible, in which the vertical shear near the base of the OSBL is weak. On the contrary, horizontal velocity in the latter pair (ST-NR and LT-NR) continues to grow as a result of the surface wind forcing, and relatively strong vertical shear near the base of the OSBL develops. The goal of having the latter pair of simulations is to contrast the effects of Langmuir turbulence on the entrainment with the effects of shear near the base of the OSBL.

For simplicity, an idealized Stokes drift profile for a monochromatic wave propagating in the same direction as the wind (x_1) is used,

$$u_1^S(x_3) = \omega k A^2 e^{2kx_3}, \quad u_2^S(x_3) = 0, \quad (2)$$

where k is the wave number, A is the wave amplitude, $\omega = \sqrt{gk}$ is the angular frequency with deep-water wave dispersion relation, and g is the gravitational acceleration. Following McWilliams *et al.* [5], a typical wave condition with $k = 0.1 \text{ m}^{-1}$ and $A = 0.8 \text{ m}$ is adopted, which gives a turbulent Langmuir number $\text{La}_r = (u^*/u^S)^{1/2} \approx 0.3$ (with u^* the friction velocity and u^S the magnitude of Stokes drift at surface) under the wind condition used here.

To minimize the inertial oscillation associated with a sudden onset of wind forcing at the beginning of the simulations, which may cause significant shear at the base of the boundary layer, ST-R and LT-R are initialized with a smooth onset of wind and Stokes forcing by applying a time filter during spin-up,

$$F(t) = \frac{1}{2} \left[1 - \cos \left(\frac{\pi t}{T_0} \right) \right], \quad 0 \leq t \leq T_0, \quad (3)$$

where $T_0 = 86400 \text{ s}$ is the spin-up time, which is $\sqrt{2}$ times the inertial period in the rotating (R) cases—slow enough to significantly reduce resonance. After spin-up, the two simulations are carried on for about 10^5 s under constant forcing to reach quasiequilibrium. For ST-NR and LT-NR, such smooth spin-up is not necessary. The OSBL depth in these two simulations starts to increase with a constant rate after about 10^4 s and the total simulation time is about 10^5 s . Unless otherwise noted, all mean profile results are averaged over the last inertial oscillation period ($T = 2\pi/f \approx 6.1 \times 10^4 \text{ s}$). The same averaging window is used for the nonrotating (NR) cases. Snapshots of velocity field shown are taken at the end of the simulations.

A summary of the four simulations is given in Table I, and the vertical profiles of the normalized horizontal mean Lagrangian velocity, vertical velocity variance, and mean vertical buoyancy flux are shown in Fig. 1. For clarity the vertical x_3 direction is normalized by the boundary layer depth h_b .

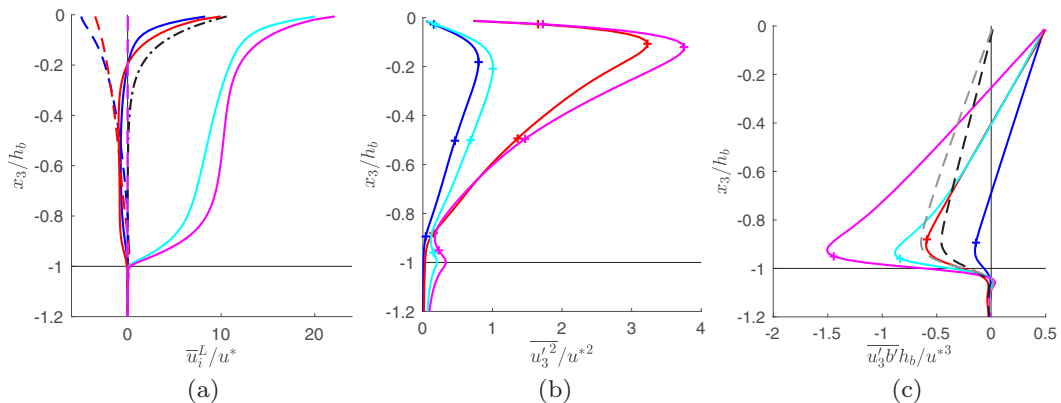


FIG. 1. Vertical profiles of the normalized (a) horizontal mean Lagrangian velocity, (b) vertical velocity variance, and (c) mean vertical buoyancy flux. Simulations ST-R, LT-R, ST-NR, and LT-NR are represented by blue, red, cyan, and magenta, respectively. Solid and dashed curves in (a) show \bar{u}_1^L and \bar{u}_2^L , and dash-dot curve in black shows the Stokes drift. Plus signs in (b) mark the four specific depths at which more analyses will be conducted to reveal the vertical variation of the turbulence structure: (1) near the surface, (2) depth at which its root-mean-square (RMS) value reaches the maximum, (3) middle of the OSBL, and (4) near the base of the OSBL. The last one is also marked in (c) to illustrate that this location lies near the maximum downward buoyancy flux. The dashed curves in (c) show the Langmuir turbulence enhanced buoyancy flux, estimated from the difference between LT-R and ST-R (black) and between LT-NR and ST-NR (gray).

No strong vertical shear is developed at the base of the OSBL in ST-R and LT-R [Fig. 1(a), blue and red]. On the contrary, significant vertical shear near the base of the OSBL is evident in both ST-NR and LT-NR [Fig. 1(a), cyan and magenta]. Near the surface, all four cases have similar Lagrangian velocity shear, but the velocities in ST-NR and LT-NR are shifted toward larger values to accommodate their near-OSBL base shear. It is expected that the near-surface turbulence structure in ST-NR resembles that in ST-R, both dominated by shear turbulence, and LT-NR resembles LT-R, both dominated by Langmuir turbulence. Indeed, such similarities and discrepancies of near-surface turbulence structure among the four cases can be inferred from the vertical velocity variance profiles, which are significantly enhanced by the presence of Langmuir turbulence in LT-R and LT-NR. However, the turbulence structure near the base of the OSBL should be different between ST-R (LT-R) and ST-NR (LT-NR) due to the different local velocity shear, limiting shear production in the R cases. This is already evident in the buoyancy flux profiles. For example, LT-R (red) and LT-NR (magenta) have very different buoyancy flux in Fig. 1(c), although their respective vertical velocity variance profiles are very similar in Fig. 1(b). Note that the small peak of vertical velocity variance at the OSBL base in ST-NR and LT-NR [Fig. 1(b)] may be due to nonbreaking internal waves, which contribute to vertical velocity variance but not entrainment, though entrainment processes may also contribute as the buoyancy flux at that level is not zero [Fig. 1(c)].

It will be examined in the next section whether Langmuir turbulence has any signature on the turbulence structure near the OSBL base, and whether the presence of strong shear alters that signature—if there is any. Note, however, that the magnitude of the Langmuir turbulence induced buoyancy flux is very similar with or without rotation, as shown by the black and gray dashed curves in Fig. 1(c). This suggests that, whatever the signature of Langmuir turbulence at the OSBL base is, its effect on the entrainment buoyancy flux may not be significantly affected by the presence of shear.

III. STRUCTURE AND ANISOTROPY OF LANGMUIR TURBULENCE

Snapshots of the normalized vertical velocity in ST-R and LT-R at four different depths, as an illustration of the turbulence structure, are shown in Fig. 2. Bands of downwelling zones in LT-R

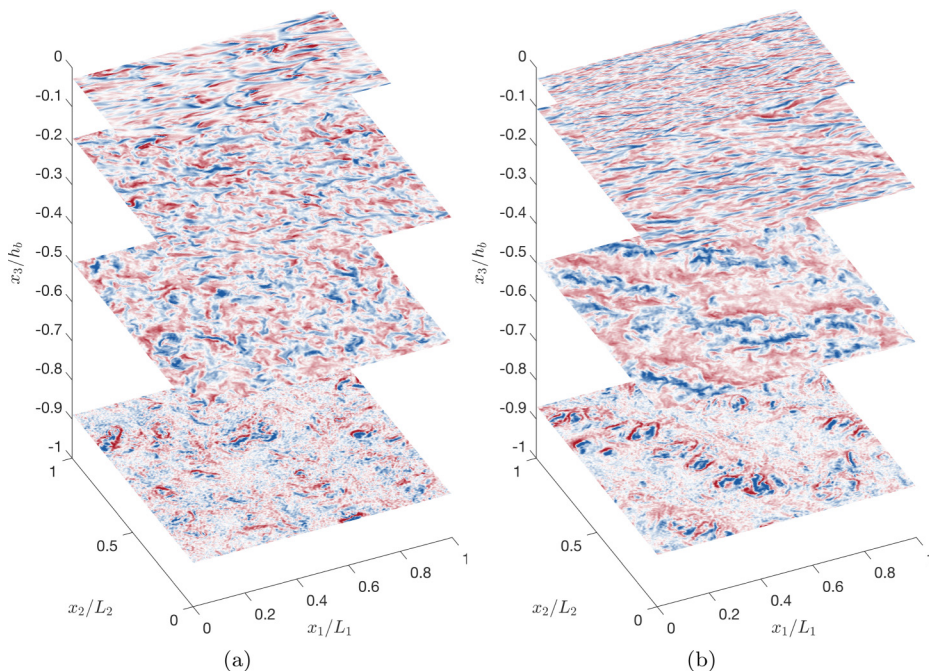


FIG. 2. Snapshots of vertical velocity for (a) ST-R and (b) LT-R at the four depths marked in Fig. 1(b). The vertical velocity is normalized by its RMS value at each depth to highlight the turbulence structure. Positive values are shown in red and negative values in blue. The horizontal and vertical axes are normalized by the horizontal dimensions of the domain (L_1 , L_2) and the boundary layer depth h_b , respectively, both defined in Sec. II B.

nearly parallel to the wind and waves (x_1 direction) near the surface, veering clockwise due to the Coriolis force and merging and increasing in spatial scales with depth [see the cross section at $x_3/h_b = -0.5$ in Fig. 2(b)], are distinctive features of Langmuir turbulence [5]. In contrast, the vertical velocity in ST-R appears more disordered. Note that although evidence of downwelling bands or waves in LT-R are noticeable at the base of the OSBL (i.e., wavelike structure are more aligned with the bands of downwelling zones), the smaller scale structure (e.g., a plume) is not so different from that in ST-R. Similar comparison can also be made between ST-NR and LT-NR as in Fig. 3, and the footprint of Langmuir turbulence near the base of the OSBL is even smaller due to the predominance of shear and internal waves there [Figs. 1(a) and 1(b)].

To quantify such similarities and discrepancies of turbulence structure seen in the vertical velocity field beyond artistic imaginings, the Reynolds stress tensor and the velocity gradient tensor will be analyzed in the following sections, which emphasize the anisotropy of turbulence and vortical structures, respectively.

A. Reynolds stress tensor and anisotropic barycentric map

The anisotropy of turbulence can be described by the anisotropy tensor [42,43], which is just the deviatoric Reynolds stress scaled by twice the TKE,

$$a_{ij} = \frac{\overline{u'_i u'_j}}{2e} - \frac{\delta_{ij}}{3}. \quad (4)$$

where $e = \overline{u'_i u'_i}/2$ is the TKE.

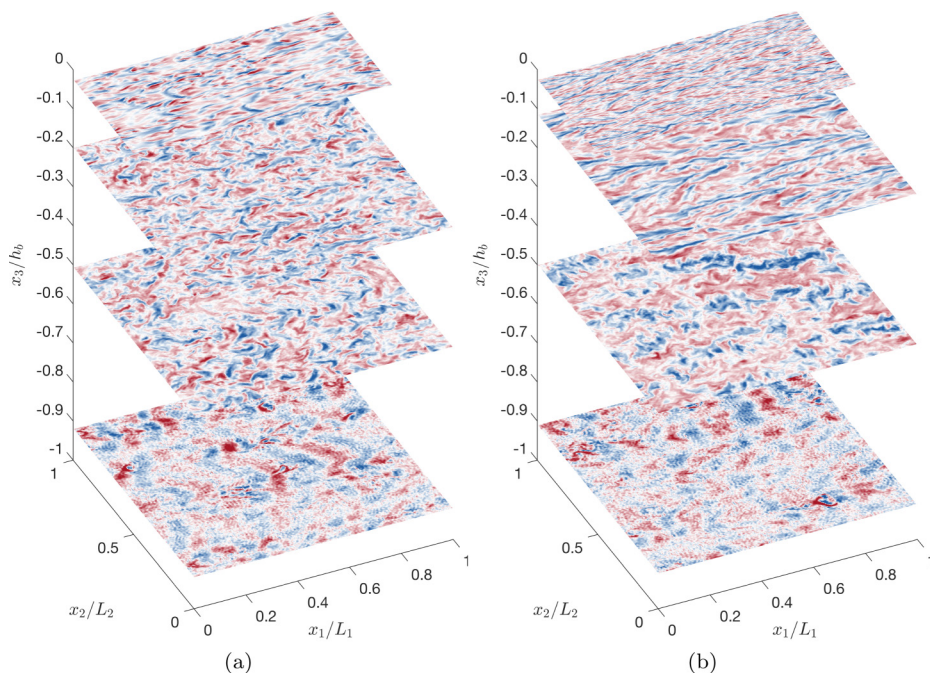


FIG. 3. Same as Fig. 2 but for (a) ST-NR and (b) LT-NR.

The three tensor invariants, i.e., the three scalar quantities that categorize the second-rank tensor a_{ij} that are unaffected by a change in coordinate system, are a useful dimensionless quantification of the geometric characteristics of turbulent structures in a flow. The first (isotropic) principal tensor invariant of a_{ij} is zero by definition [due to cancellation with the isotropic second term in (4)], i.e., $I = a_{ii} = 0$. The second and third principal invariants of a_{ij} ,

$$II = a_{ij}a_{ji}, \quad III = a_{ij}a_{jk}a_{ki}, \quad (5)$$

when plotted against each other in the anisotropy invariant map (also known as the *Lumley triangle*), describe the level of turbulence anisotropy [42,44]. This technique has been used to quantify anisotropy of Langmuir turbulence versus shear turbulence in both observations and LES of a shallow coastal region [22,36]. Alternatively and equivalently, one can use a barycentric map derived from the eigenvalues of a_{ij} , which is easier to read than the Lumley triangle [45] and proves useful in categorizing structures in tidally generated turbulence [46]. The idea is to represent any anisotropy tensor (in its rotated and reordered form, \hat{a}_{ij}) as a convex combination of three limiting states,

$$\hat{a}_{ij} = \text{diag}(\lambda_1, \lambda_2, \lambda_3) = C_{1c}\hat{a}_{1c} + C_{2c}\hat{a}_{2c} + C_{3c}\hat{a}_{3c}, \quad (6)$$

where λ_1, λ_2 , and λ_3 are the eigenvalues of a_{ij} in descending order, and

$$\hat{a}_{1c} = \text{diag}(2/3, -1/3, -1/3), \quad (7)$$

$$\hat{a}_{2c} = \text{diag}(1/6, 1/6, -1/3), \quad (8)$$

$$\hat{a}_{3c} = \text{diag}(0, 0, 0), \quad (9)$$

represent the one-component, two-component, and three-component limiting states, respectively. Here $\text{diag}(d_1, d_2, \dots, d_n)$ represent a n -by- n diagonal matrix with main diagonal entries d_1, d_2, \dots ,

d_n . The normalizing coefficients $\{C_{1c}, C_{2c}, C_{3c}\}$ are chosen in a manner such that,

$$C_{1c} + C_{2c} + C_{3c} = 1, \quad \{C_{1c}, C_{2c}, C_{3c}\} \in [0, 1]. \quad (10)$$

They are related to the eigenvalues of a_{ij} by

$$C_{1c} = \lambda_1 - \lambda_2, \quad (11)$$

$$C_{2c} = 2(\lambda_1 - \lambda_2), \quad (12)$$

$$C_{3c} = 3\lambda_3 + 1. \quad (13)$$

A barycentric map can be drawn given the barycentric coordinates $\{C_{1c}, C_{2c}, C_{3c}\}$. The position of a point in the barycentric map then illustrates how close the turbulence state is to each of the three limiting states. For example, a point with the barycentric coordinates of $\{0, 0, 1\}$ is on the vertex labeled as “3 comp” in Fig. 4(a), corresponding to pure three-component (or isotropic) turbulence. The vertices labeled as “2 comp” and “1 comp” in Fig. 4(a) correspond to pure two-component and pure one-component turbulence, respectively, with the former having equal velocity fluctuations in two directions and zero in the other, and the latter having nonzero velocity fluctuations only in one direction. The three edges labeled as “axisymmetric expansion”, “axisymmetric contraction”, and “two component” show the transition paths between any two of the three limiting states. The “Plane strain” limit ($III = 0$ in Lumley triangle) shows a special path between the three-component and the two-component states along which the velocity fluctuation in one direction is constant. More detailed discussion and comparison with the Lumley triangle is given by Banerjee *et al.* [45].

While the anisotropic barycentric map illustrates the level of anisotropy by using the eigenvalues of a_{ij} , because these eigenvalues are scalars and thus insensitive to coordinate systems, the barycentric map does not inform the directions of principal axes of anisotropy when it exists, which are determined by comparing the eigenvectors of a_{ij} to other key directions in the physical situation, such as the direction of the local vertical, gravity, the down-wind or Lagrangian shear direction. A natural extension of the anisotropic barycentric map includes the directional information of the anisotropy by reference to these key broken symmetries.

There are three eigenvectors of a_{ij} , $\{\hat{\mathbf{v}}_1, \hat{\mathbf{v}}_2, \hat{\mathbf{v}}_3\}$, associated with the three eigenvalues, $\{\lambda_1, \lambda_2, \lambda_3\}$. However, it is not necessary to show all their directions. Indeed, directions are important only for two limiting states of anisotropy: one component and two component, for which the directions of interest are along the major axis (the orientation of the one-component turbulence) and minor axis (the orientation of the axis perpendicular to the planar, or transversely isotropic, turbulence), respectively. To illustrate the direction of anisotropy we will only need the direction of the major axis for nearly one-component (N1C) regime, or *cigarlike*, and the minor axis for nearly two-component (N2C) regime, or *pancakelike*. The direction of interest for each regime and the criterion distinguishing these two are

$$\begin{aligned} \text{N1C, Major axis,} & \quad \text{if } C_{1c} > C_{2c}, \\ \text{N2C, Minor axis,} & \quad \text{if } C_{1c} < C_{2c}. \end{aligned} \quad (14)$$

Note that we use different symbols to mark the direction of the major (\circ) and minor (\times) axes in Figs. 4(b) and 4(d) and Figs. 5(b) and 5(d). The terms *cigarlike* and *pancakelike* describe the relative magnitude of velocity fluctuations along three principal axes, not the spatial scales in a typical visualization of coherent structures. For example, the elongated rolls typical of Langmuir circulations are pancakelike in terms of velocity fluctuations (or the Reynolds stresses), for which the minor axis points to the axis direction of the rolls.

The direction of a unit vector in three-dimensional space can be represented by two angles: the *azimuth*, or horizontal angle away from a chosen horizontal direction, θ , and the *elevation* angle above the local horizontal toward the zenith, ϕ . These two directions play equivalent roles to longitude and latitude, respectively, in a local spherical coordinate system. The directions of interest

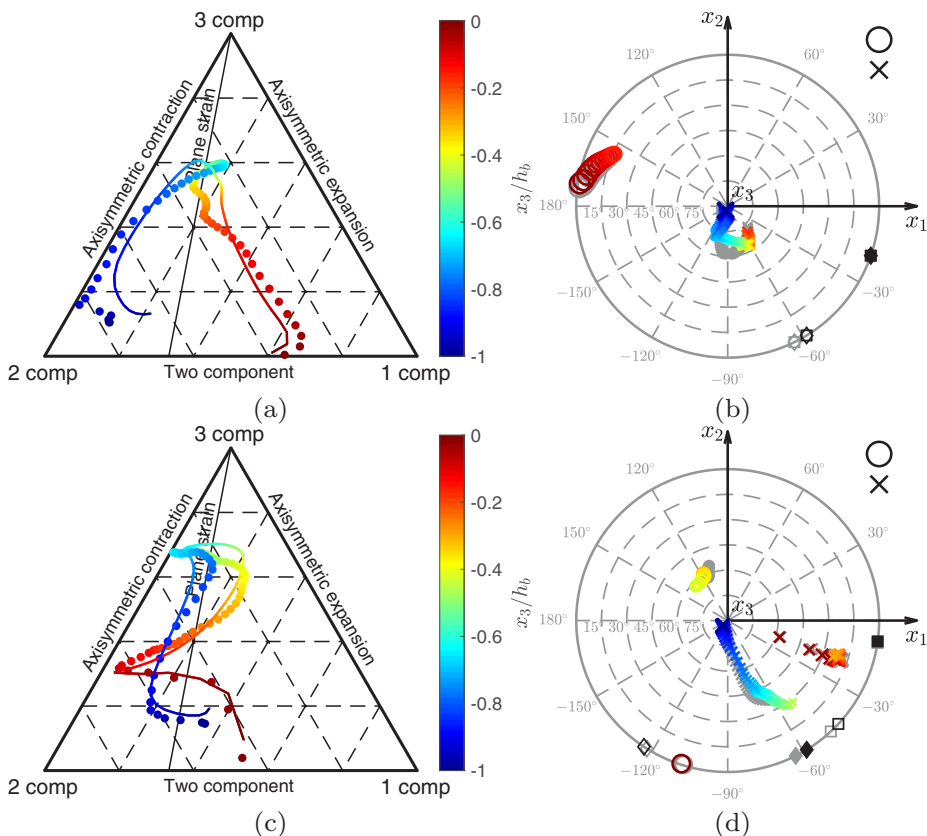


FIG. 4. Left panels show the anisotropic barycentric map as a function of normalized depth, x_3/h_b (color), for simulations (a) ST-R and (c) LT-R. Colored dots show the anisotropy of the instantaneous, horizontally averaged Reynolds stresses at the end of the simulation, whereas solid curves show the Reynolds stresses averaged horizontally over space and averaged over time over the last inertial period. Right panels show the direction of anisotropy as a function x_3/h_b for (b) ST-R and (d) LT-R, using the same color scheme to indicate depth for reference to (a) and (c). The direction of major axis (greatest eigenvalue) is marked by circles for cigarlike (longitudinal) structure, whereas the direction of minor axis (smallest eigenvalue) is marked by crosses for pancakelike (transverse) structure, with color for the instantaneous flow and gray for the mean flow. The size of the markers is proportional to the degree of anisotropy (see more details in the text). Black circle and cross in the upper right corner show the sizes corresponding to pure one-component and two-component turbulence. Filled squares and diamonds at the edge mark the mean direction of $\langle \partial \bar{u}_i^t / \partial x_3 \rangle_{0.25h_b}$ and $\langle \partial \bar{u}_i / \partial x_3 \rangle_{0.25h_b}$, respectively, averaged over the upper 25% of the boundary layer for the instantaneous flow (black) and mean flow (gray). Empty squares and diamonds at the edge mark the mean direction of $\langle \bar{u}_i^t \rangle_{0.25h_b}$ and $\langle \bar{u}_i \rangle_{0.25h_b}$, respectively.

here are the along-wind (x_1 direction, the direction of wind and waves in these simulations and the direction of mean flow in the nonrotating simulations), cross-wind (x_2 direction), and vertical (x_3 direction) directions. The azimuth angle θ measures the along-wind versus cross-wind directionality, while the elevation angle ϕ measures horizontal versus vertical. Both angles illustrating the direction of anisotropy can be shown in a two-dimensional map as is done in Fig. 4(b). Black arrows indicate the along-wind (x_1) and cross-wind (x_2) directions, with labels on the edge of the gray circle showing θ . The x_3 direction is represented by the center of the gray concentric circles (pointing out of the paper), with the labels on each concentric dashed circle showing the value of ϕ indicating horizontal versus vertical orientation of the unit vector direction of anisotropy. Here we

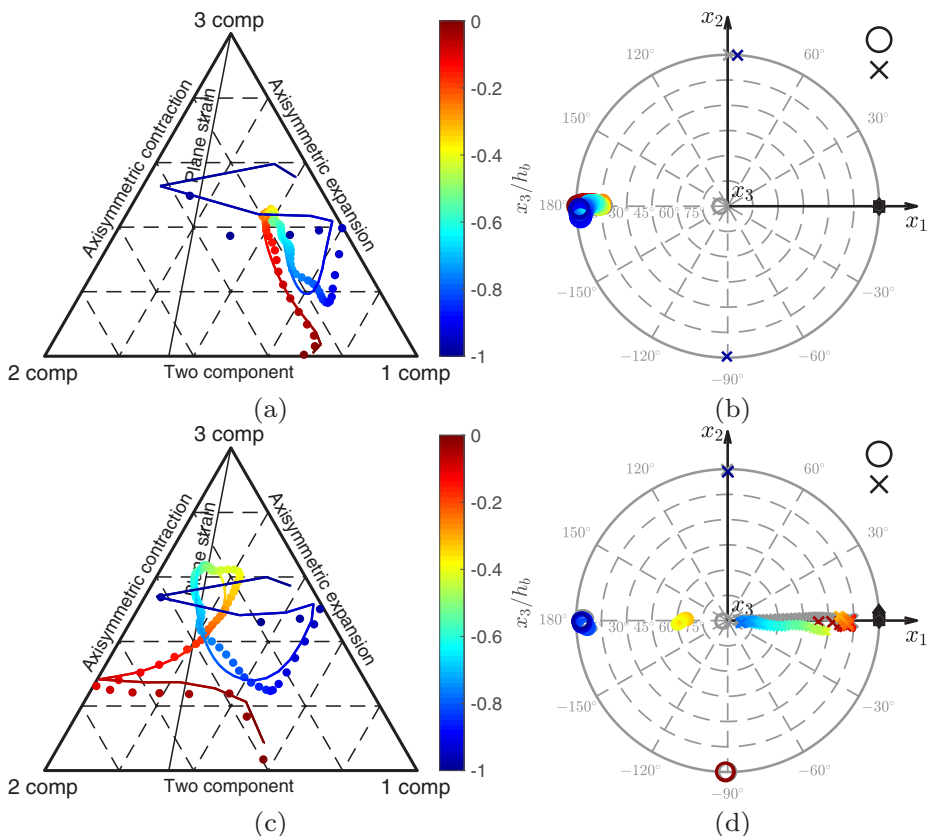


FIG. 5. Same as Fig. 4, but for [(a) and (b)] ST-NR and [(c) and (d)] LT-NR.

are not distinguishing between positive and negative along a particular direction, so that pointing up and upwind is equivalent to pointing down and downwind [e.g., dark red circles in Fig. 4(b)].

Note that the absolute value of C_{1c} and C_{2c} measure the level of one- and two-component anisotropy. When both $C_{1c} \rightarrow 0$ and $C_{2c} \rightarrow 0$, three-component regime is approached and then directional information becomes irrelevant. The relevance of the directional information should then be weighted by the level of anisotropy. To emphasize greater anisotropy, we set the marker size for the major and minor axis directions proportional to the magnitude of C_{1c} and C_{2c} , respectively. Then the relevance of the direction is illustrated by the marker size and the marker automatically vanishes for three-component turbulence.

For horizontally homogeneous turbulence in the LES, the level of anisotropy can be analyzed at each depth to illustrate the structure of turbulence throughout the OSBL. Figure 4 shows the anisotropic barycentric map and direction of anisotropy for simulations ST-R and LT-R, respectively, as a function of the normalized depth x_3/h_b . Color marks the depth, with red showing the surface and blue showing the base of the OSBL. Both the instantaneous flow field at the end of the simulation and the mean flow field averaged over the last inertial period are analyzed, shown by the dots and solid curves, respectively. For clarity the direction of anisotropy for the mean flow are shown in gray. Note that the sudden jump in the orientation angle as depth increases in Figs. 4(b) and 4(d) is a result of showing the direction of major and minor axes for N1C and N2C regimes, respectively. Both the level of anisotropy and its direction, as well as their vertical structures throughout the OSBL, are generally consistent between the instantaneous flow and mean flow. This suggests that the statistics of turbulence structure from a horizontal average of the instantaneous flow is representative of the temporally averaged statistics.

Comparison between Figs. 4(a) and 4(b) and Figs. 4(c) and 4(d) reveals the differences in the anisotropy between ST-R and LT-R, especially near the surface where substantial Stokes shear exists in LT-R but not ST-R (Fig. 1). At the surface, though both exhibit two-dimensional structure primarily due to the blocking effect where motions in the vertical direction are suppressed, the dominant directions are different, namely along-wind for ST-R versus cross-wind for LT-R (dark red circles). Right below the surface, turbulence in LT-R (red crosses) indicates a pancakelike turbulence with a minor direction being nearly along-wind, which is a direct result of the tilted counter-rotating vortices about an axis oriented along the shear direction typical of Langmuir turbulence [47]. Those tilted counter-rotating vortices correspond more with the near-surface mean Lagrangian shear, $\langle \partial \bar{u}_i^L / \partial x_3 \rangle_{0.25h_b}$ (filled squares), than the mean Eulerian shear, $\langle \partial \bar{u}_i / \partial x_3 \rangle_{0.25h_b}$ (filled diamonds), consistent with the vortex tilting and stretching mechanisms of Langmuir circulation [9,37,47]. Note that the near-surface averaged Lagrangian shear and Eulerian shear are deflected to the right of the wind direction by the Coriolis force, though the shear exactly at the surface is aligned with the wind. These features in anisotropy distinguish Langmuir turbulence from the shear-induced turbulence near the surface, which exhibits a cigarlike structure as in ST-R. Near the base of the OSBL, however, both ST-R and LT-R exhibit pancakelike structure about a minor axis direction that is nearly vertical, though quantitative differences between $x_3/h_b = -0.5$ and $x_3/h_b = -0.8$ are noticeable. In addition, in both ST-R and LT-R these structures tilt towards the direction of the mean surface Lagrangian velocity, $\langle \bar{u}_i^L \rangle_{0.25h_b}$, which suggests a mean vertical shear $\sim \langle \bar{u}_i^L \rangle_{0.25h_b} / h_b$ is important in breaking the azimuthal symmetry in both cases. These results show that the distinctive features of the anisotropy of Langmuir turbulence are not retained at the base of the OSBL.

Similarly, significant distinctions near the surface and general similarities at the base of the OSBL in the anisotropy of turbulence are also observed in ST-NR and LT-NR, as illustrated by Fig. 5. The primary difference is that in these two simulations there exists a strong mean vertical shear near the base of the OSBL. As a result, the turbulence there in both cases exhibit cigarlike structure in the along-wind direction, just like those structures near the surface induced by the surface shear in ST-R and ST-NR. Again, the distinctive pancakelike structure of Langmuir turbulence tilted to align with the Lagrangian shear (along-wind in LT-NR) does not extend to the base of the OSBL, ending near $x_3/h_b = -0.4$.

Near the surface, the key distinction in anisotropy is based on whether or not there is Stokes shear. Comparing the near-surface (red to yellow crosses) Langmuir turbulence simulation pair in LT-R [Fig. 4(d)] and LT-NR [Fig. 5(d)] illustrates the Langmuir turbulence orientation, while the distinctive leftward cusp (reddish symbols) across the plane strain line in LT-R [Fig. 4(c)] and LT-NR [Fig. 5(c)] shows the change in anisotropy with depth across the Stokes shear typical of this Langmuir turbulence. The shear turbulence pair of cases ST-R [Fig. 4(a)] and ST-NR [Fig. 5(a)] lack this cusp in their near-surface anisotropy (reddish symbols).

Near the OSBL base, the key distinction in anisotropy relies on whether there is Eulerian shear, which depends on rotating versus nonrotating scenarios. Comparison between Fig. 4 and Fig. 5 reveals the differences in the turbulence anisotropy at the base of the OSBL in the two entrainment regimes, i.e., a “plume regime” where downward TKE transport associated with deep penetrating plumes may provide the energy for entrainment of denser water from below, and a “shear regime” where shear production by the local shear-induced instabilities may provide the energy for entrainment. At depth (bluer symbols), the opposite pairing to that at the surface occurs in anisotropy, where ST-R [Fig. 4(a)] and LT-R [Fig. 4(c)] resemble one another and ST-NR [Fig. 5(a)] and LT-NR [Fig. 5(c)] resemble one another. As if in a square or group dance, the turbulence partners that pair at the surface are traded over depth for the other pairing of partners at the OSBL base. So, in both regimes, the presence or absence of Langmuir turbulence that dominates near the surface does not significantly affect the turbulence anisotropy and structure near the base of the OSBL, which is governed by the Eulerian shear distinction between rotating and nonrotating partner pairs.

Note that these results are not inconsistent with the fact that the downwelling plumes may be somewhat more organized (e.g., they tend to be aligned into parallel bands) in the presence of Langmuir turbulence Fig. 2. However, when averaged over a domain much larger than the individual

plumes, as is the case here to emphasize on the mean effects, these more organized structures do not affect the turbulence anisotropy as seen in Figs. 4 and 5. Great care is therefore required when applying the same analysis to a smaller domain. It is likely that higher order statistics (e.g., the triple correlation or third-order structure function) would reflect these distinctions, while the second-order covariances of the Reynolds stresses are relatively insensitive.

B. Velocity gradient tensor and invariant diagram

While the invariants of the Reynolds stress tensor are useful in describing the anisotropy of turbulence, the invariants of the velocity gradient tensor are commonly used to identify and describe the structures of turbulent flows (e.g., Refs. [48–51]). The velocity gradient tensor can be broken into a symmetric and an antisymmetric part, $T_{ij} = \partial u_i / \partial x_j = S_{ij} + A_{ij}$, where $S_{ij} = (T_{ij} + T_{ji})/2$ and $A_{ij} = (T_{ij} - T_{ji})/2$ are the rate-of-strain and rate-of-rotation tensors, respectively. For an incompressible fluid, the three matrix invariants of T_{ij} are

$$P = -T_{ii} = 0, \quad (15)$$

$$Q = -\frac{1}{2}T_{ij}T_{ji} = -\frac{1}{2}(S_{ij}S_{ji} + A_{ij}A_{ji}) = \frac{1}{2}(A_{ij}A_{ij} - S_{ij}S_{ij}), \quad (16)$$

$$R = -\frac{1}{3}T_{ij}T_{jk}T_{ki} = \frac{1}{3}(-S_{ij}S_{jk}S_{ki} - 3A_{ij}A_{jk}S_{ki}). \quad (17)$$

The invariants of S_{ij} are defined by letting $A_{ij} = 0$ in (15)–(17), i.e., $P_S = 0$, $Q_S = -\frac{1}{2}S_{ij}S_{ij}$, and $R_S = -\frac{1}{3}S_{ij}S_{jk}S_{ki}$. The first and third invariants of A_{ij} are identically zero. So the only nonzero invariant of A_{ij} is $Q_A = \frac{1}{2}A_{ij}A_{ij}$ and is related with Q and Q_S by $Q = Q_S + Q_A$. Note the close relation of Q to the Okubo-Weiss parameter in 2D flow, which is strain rate squared minus vorticity squared [52–55]. Q is a vector-invariant, arbitrary-dimensionality generalization of the same concept.

Those invariants, when plotted against each other, provide abundant information on the topology of flow patterns (e.g., Refs. [48,49]). Commonly used pairs include (R, Q) , (R_S, Q_S) , and $(Q_A, -Q_S)$. We are going to focus on the last pair, $(Q_A, -Q_S)$, as it effectively distinguishes shear structures from vortical structures.

To see this, consider the fact that $Q_A = \frac{1}{2}A_{ij}A_{ij} = \frac{1}{4}\omega_i\omega_i$, with $\omega_i = \epsilon_{ijk}T_{kj}$ the vorticity, is proportional to the enstrophy density which represents the strength of rotation, whereas $-Q_S = \frac{1}{2}S_{ij}S_{ij} > 0$ is proportional to the local dissipation of kinetic energy. Regions of large Q_A correspond to structures with strong rotation, either vortex tubes or vortex sheets. On the other hand, regions of large $-Q_S$ correspond to strong strain, either rotational or irrotational. Therefore, co-occurrence of large Q_A and large $-Q_S$ indicates a predominance of vortex sheets, with large Q_A and small $-Q_S$ a predominance of vortex tubes, and small Q_A and large $-Q_S$ a predominance of irrotational dissipation. For the same reason, isosurfaces of positive Q ($Q_A > -Q_S$) are commonly used to visualize vortex tubes in a turbulent flow field (e.g., Ref. [51]).

Figure 6 shows the joint distribution of normalized Q_A and $-Q_S$ for the four simulations (columns) in different depth ranges throughout the OSBL (rows). Consistent with the structures revealed by the analyses of turbulence anisotropy, the distinctive features of Langmuir turbulence only exist within the surface 25% of the OSBL where Stokes shear is significant. For example, evidence of vortex tubes is observed near the surface in LT-R and LT-NR, but not in ST-R and ST-NR, where vortex sheets predominate. Near the base of the OSBL, turbulence structures look quite similar between ST-R and LT-R, and between ST-NR and LT-NR, respectively, with evidence of combined vortex tubes and vortex sheets in the former pair, and predominance of vortex sheets in the latter pair. In the middle of the OSBL, where no strong shear exists, turbulence structures look very similar among all four simulations. The group dance, where partners are traded with depth, also appears in the statistics of the velocity gradient.

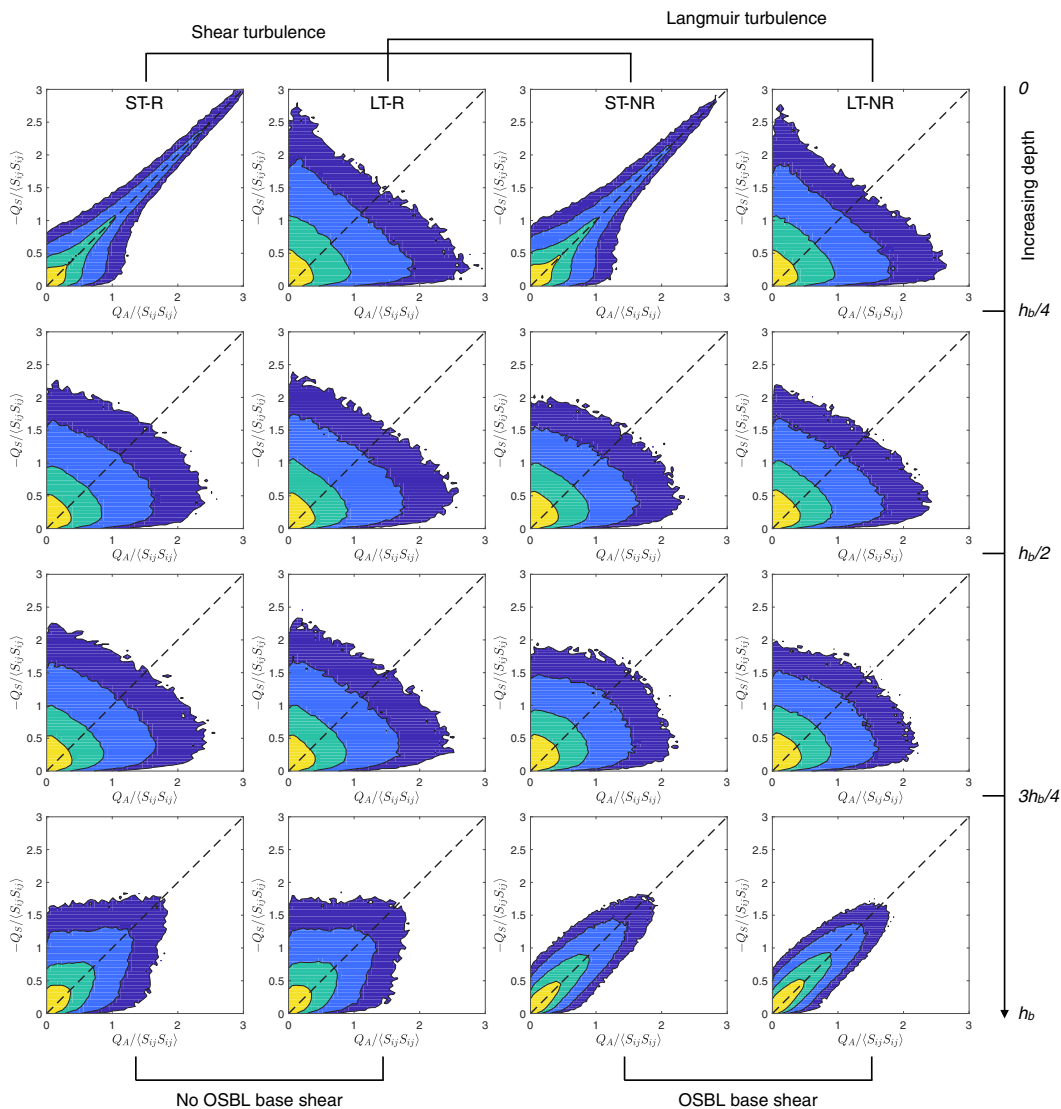


FIG. 6. Joint distribution of normalized Q_A and $-Q_S$ for different simulations in different depth ranges. Columns, from left to right, show results of ST-R, LT-R, ST-NR, and LT-NR, respectively. Rows, from top to bottom, show statistics within the four quarters of the boundary layer, respectively. Yellow, green, light blue, and dark blue show the highest 50, 75, 90, and 95% centered distribution, respectively. For example, 50% of all occurrence in the parameter space with the highest probability density is shown in yellow.

IV. ENTRAINMENT

The entrainment at the base of the OSBL is strongly affected by the structure and anisotropy of the turbulence, which determine the partition of the available TKE at the base of the OSBL into potential energy creation (i.e., mixing) and dissipation. To demonstrate this, Fig. 7 shows the joint distributions of normalized vertical velocity and buoyancy fluctuations at the entrainment level [as marked in Fig. 1(c)] for all four cases. Both vertical velocity and buoyancy fluctuations are normalized by their standard deviation to highlight their correlations instead of their magnitudes, which are quite different as expected. The joint distributions are estimated from the time series

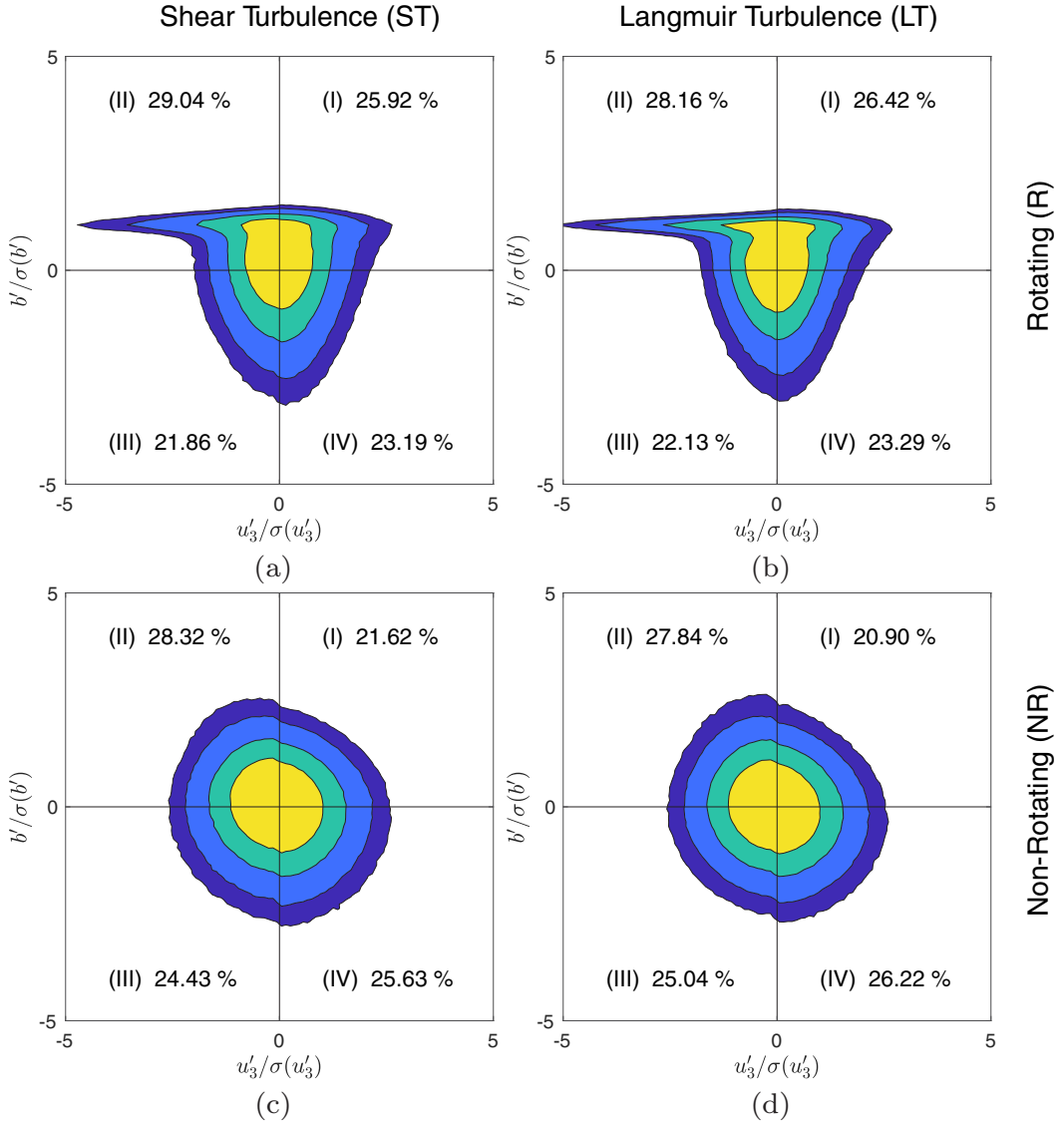


FIG. 7. The joint distribution of the normalized fluctuations of vertical velocity and buoyancy at the entrainment level ($x_3 \approx -0.9h_b$) for (a) ST-R, (b) LT-R, (c) ST-NR, and (d) LT-NR. The fluctuations of both variables are normalized by their standard deviation. Yellow, green, light blue, and dark blue show the highest 50, 75, 90, and 95% centered distribution, respectively. The numbers at each quadrant shows the fractional area of (I) rarefied updraft, (II) rarefied downdraft, (III) dense downdraft, and (IV) dense updraft.

of the buoyancy flux snapshots at the entrainment level taken approximately every 3 min over the analyzing window (the last $\sim 6.1 \times 10^4$ s of the simulations). Four quadrants of each panel show the four regimes that contribute to the entrainment: (I) rarefied updraft, (II) rarefied downdraft, (III) dense downdraft, and (IV) dense updraft. A negative entrainment buoyancy flux as in all four cases may result from either light downdraft or dense updraft.

The resulting probability density function (PDF) of entrainment buoyancy flux for the four cases are shown in Fig. 8. Again, the entrainment buoyancy fluxes are normalized by their standard deviation to emphasize the shape of the distribution and to allow direct comparison among different

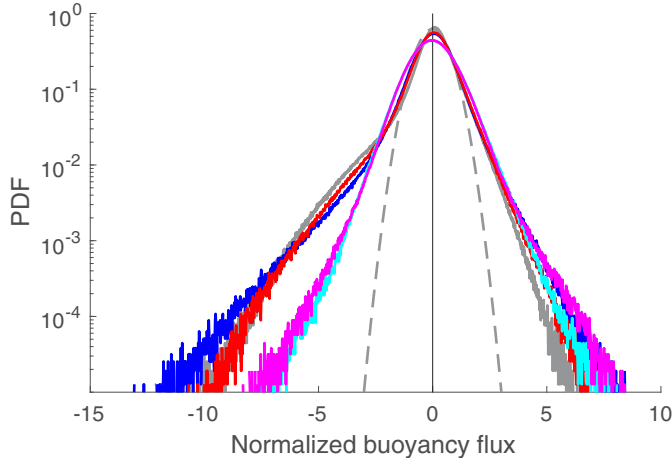


FIG. 8. The PDF of normalized entrainment buoyancy flux. Solid curves in blue, red, cyan and magenta show the results of ST-R, LT-R, ST-NR, and LT-NR, respectively. The same PDF for a pure convection case is shown in gray. An arbitrary normal distribution is shown by the dashed curve for reference. Note the logarithmic scale in the vertical axis.

cases. Note again that their mean values and standard deviations are significantly different [see Fig. 1(c)]. In addition to the four cases analyzed in this study, the same PDF for a pure convection case, in which convective plumes energize the entrainment, is shown in gray as a reference. The PDFs are plotted in logarithmic scale to highlight the extreme values whose asymmetry between positive and negative leads to the net negative entrainment buoyancy flux as shown in Fig. 1(c).

Similarities and discrepancies among the four cases are immediately evident, reminiscent of those in the turbulent velocity gradient statistics structure at the base of the OSBL shown in the previous section. As this is a statistic of the OSBL base turbulence, the PDF of LT-R resembles that of ST-R, and LT-NR resembles ST-NR, while the two pairs differ a lot from each other. The entrainment processes in ST-R and LT-R are dominated by plumelike structures that resemble convective plumes, indicated by the exceptionally strong rarefied downdrafts shown in the upper left quadrant (II) of Figs. 7(a) and 7(b). The partitioning of the joint distribution of vertical velocity and buoyancy fluctuations in ST-NR and LT-NR are more symmetric among the rarefied updraft, rarefied downdraft, dense downdraft and dense updraft. This is due to the predominance of nonbreaking internal waves in these cases: Linear internal plane waves would be equally partitioned among the quadrants. As a result, the PDFs of entrainment buoyancy flux in ST-NR and LT-NR both have a more symmetric shape and the entrainment is less efficient than the plumelike structure in ST-R and LT-R.

The resemblances between ST-R and LT-R, and between ST-NR and LT-NR, in both Fig. 7 and Fig. 8 suggest that the presence of Langmuir turbulence does not appear to affect the predominant character of processes that drive the entrainment or turbulence statistics near the OSBL base. On the other hand, Stokes drift versus shear forcing dominates the near-surface normalized statistics. However, despite the similarities in *normalized, dimensionless* turbulence metrics near the OSBL base (Figs. 4–8), significant differences of the net entrainment buoyancy flux in Langmuir versus shear cases remain as shown in Fig. 1(c). Therefore, the Langmuir turbulence enhanced entrainment appears to be a result of extra energy through enhanced downward TKE transport (e.g., Refs. [5,27]) without major changes to the structural character or normalized turbulence statistics. The implication for parametrizations of turbulence covariances and their effects and dependence on mean shear is that an existing OSBL model (e.g., KPP) can be modified in a straightforward way to incorporate the effects of Langmuir turbulence on entrainment [per 23]. In the regime of weak

shear at the OSBL base (ST-R and LT-R), this can be achieved mostly by enhancing entrainment due to unresolved shear associated with the plumelike structures of the deeply penetrating jets [30], which is the approach taken in Li and Fox-Kemper [23]. In the regime of strong shear at OSBL base (ST-NR and LT-NR), enhanced entrainment may also result from enhanced shear-induced mixing as reported in Kukulka *et al.* [33].

V. DISCUSSION AND CONCLUSIONS

Structure and anisotropy of turbulence in four LES experiments simulating the OSBL, with and without Stokes forces, with and without rotation, are analyzed. Similarities and distinctions between Langmuir turbulence and shear turbulence throughout the OSBL are highlighted. This study distinguishes itself from previous studies of similar topics such as Li *et al.* [11] and Teixeira and Belcher [12] by its emphasis on the turbulence structure and anisotropy near the base of the OSBL and their relation to the Langmuir turbulence-enhanced mixed layer entrainment, as well as employing newer and cleaner diagnostic methods.

The anisotropic barycentric maps with accompanying eigenvector direction maps are demonstrated to be useful diagnostics for identifying the turbulence structure from the Reynolds stresses. Though gridded model data are used in this demonstration, these diagnostics can potentially be applied to observational data, such as the Reynolds stress measured by an acoustic Doppler velocimeter (e.g., Refs. [46,56,57]), or even a five-beam acoustic Doppler current profiler if the turbulent structures are sufficiently large to have velocity covariances across the beam spread as used by Gargett *et al.* [22] in coastal regions. The agreement between results from temporally and horizontally averaged Reynolds stresses and from snapshots of velocity field suggests the robustness of these diagnostics. MATLAB tools to generate these diagnostics from Reynolds stresses are hosted on Github [58].

Consistent with previous studies, Langmuir turbulence has distinctive structures and anisotropy near the surface of the OSBL versus those of shear turbulence. In particular, Reynolds stresses of Langmuir turbulence exhibit pancakelike structure with a minor direction nearly down-wind and waves near the surface, in contrast to Reynolds stresses of shear turbulence which exhibit cigarlike structure with a down-wind major direction. Note again that we are using these geometrical terms (e.g., pancakelike and cigarlike) in this paper to describe the turbulence anisotropy in velocity fluctuations, in contrast to the anisotropy in spatial scales in a typical visualization of turbulence structures. These features illustrated in the anisotropic barycentric maps and directional maps are further confirmed by the vortex tubes and vortex sheets structures in the velocity gradient invariant diagrams for Langmuir turbulence and shear turbulence, respectively.

Such distinctive features of Langmuir turbulence are direct results of the Stokes-vortex force or Stokes shear force exerted by the Stokes drift shear [9,10], and can also be understood using the rapid distortion theory [12,37]. The statistics connected to these distinctive features are quickly lost at depths below where the Stokes drift shear is significant, though somewhat more organized larger scale structure associated with the downward jet of the Langmuir cells are still noticeable throughout the OSBL. This disappearance with depth probably explains the open ocean observations in which no significant structural evidence of Langmuir circulation was found in the lower half of a 40 to 60 m OSBL (e.g., Refs. [24,25]), as the coherent structures of Langmuir turbulence may have been too weak to be observed there. Nonetheless, the results here indicate that the near-surface Langmuir turbulence may energize the turbulence below without changing most of its low-order *normalized* statistics.

Therefore, the presence of Langmuir turbulence does not seem to strongly affect the structure and normalized statistics of the predominant processes at the base of the OSBL that drive entrainment. However, this conclusion does not imply that Langmuir turbulence has no effect on the entrainment. Enhanced entrainment is commonly seen in LES with Langmuir turbulence [5,23,27]. Instead, such Langmuir turbulence-enhanced entrainment results from extra energy supply, which animations of the simulations indicate are due to enhanced downward TKE transport by more frequent and more

energetic downward plumes and through enhanced vertical shear near the OSBL base resulting from enhanced downward momentum transport above (Fig. 1).

The implication of these results for parametrizing the entrainment process at the base of the OSBL is that small scale turbulence that induces entrainment does not depend significantly on the form of energy source near the surface, i.e., wind, waves or convection. The difference, however, is how efficient the energy being transported down to the base, which determines how much energy is available to lift the denser water from below the OSBL. Existing models for entrainment based on conservation of energy, convective plumes or local shear instabilities can therefore be easily modified to incorporate the effects of Langmuir turbulence by just increasing the energy sources. Examples of this approach include Li and Fox-Kemper [23] and Reichl and Li [59].

Here the effects of Langmuir turbulence on entrainment are assessed in two limiting regimes where the shear at the base of the OSBL is either strong or negligible. This corresponds to entrainment induced by resolved and unresolved shear parameterized separately in first moment closure models such as KPP. A mixture between these two limiting regimes is probably more common in reality. A direct step forward would apply the same analysis and metrics illustrated here on more realistic LES cases with surface forcing of mixed wind, wave and surface buoyancy flux so that the transitioning of turbulence structure and anisotropy can be studied. Such knowledge is also relevant to the second moment closure models of Langmuir turbulence, such as Harcourt [60] and Harcourt [61], and these closures might also selectively drive consideration of higher-order statistics. For example, the closure of the pressure-strain rate correlations in second moment closure models depends on assumptions of the rate of return-to-isotropy [62], which differ for different types of anisotropic turbulence (e.g., Ref. [44]). The return-to-isotropy term may also need to be modified for Langmuir turbulence in addition to the distortion term as in Harcourt [60] and Harcourt [61].

ACKNOWLEDGMENTS

We thank Eric D'Asaro and an anonymous reviewer for their very useful input on this manuscript, whose comments greatly helped to clarify our presentation. Support from NSF Grants No. 1258907 and No. 1350795 and ONR Grant No. N00014-17-1-2963 is gratefully acknowledged. All the LES runs were conducted using computational resources and services at the Center for Computation and Visualization, Brown University, supported in part by the National Science Foundation EPSCoR Cooperative Agreement EPS-1004057. We are grateful to Peter Sullivan for making the LES code available.

-
- [1] G. L. Mellor and T. Yamada, Development of a turbulence closure model for geophysical fluid problems, *Rev. Geophys. Space Phys.* **20**, 851 (1982).
 - [2] W. G. Large, J. C. McWilliams, and S. C. Doney, Oceanic vertical mixing: A review and a model with a nonlocal boundary layer parameterization, *Rev. Geophys.* **32**, 363 (1994).
 - [3] H. Burchard, P. D. Craig, J. R. Gemmrich, H. van Haren, P.-P. Mathieu, H. E. M. Meier, W. A. M. N. Smith, H. Prandke, T. P. Rippeth, E. D. Skillingstad, W. D. Smyth, D. J. S. Welsh, and H. W. Wijesekera, Observational and numerical modeling methods for quantifying coastal ocean turbulence and mixing, *Prog. Oceanogr.* **76**, 399 (2008).
 - [4] E. A. D'Asaro, Turbulence in the upper-ocean mixed layer, *Annu. Rev. Mar. Sci.* **6**, 101 (2014).
 - [5] J. C. McWilliams, P. P. Sullivan, and C.-H. Moeng, Langmuir turbulence in the ocean, *J. Fluid Mech.* **334**, 1 (1997).
 - [6] G. G. Stokes, On the theory of oscillatory waves, *Trans. Cambr. Philos. Soc.* **8**, 441 (1847).
 - [7] K. E. Kenyon, Stokes drift for random gravity waves, *J. Geophys. Res.* **74**, 6991 (1969).
 - [8] T. S. van den Bremer and Ø. Breivik, Stokes drift, *Philos. Trans. R. Soc. A* **376**, 20170104 (2018).
 - [9] A. D. D. Craik and S. Leibovich, A rational model for Langmuir circulations, *J. Fluid Mech.* **73**, 401 (1976).

- [10] N. Suzuki and B. Fox-Kemper, Understanding Stokes forces in the wave-averaged equations, *J. Geophys. Res.: Oceans* **121**, 3579 (2016).
- [11] M. Li, C. Garrett, and E. D. Skillingstad, A regime diagram for classifying turbulent large eddies in the upper ocean, *Deep-Sea Res. Part I: Oceanogr. Res. Pap.* **52**, 259 (2005).
- [12] M. A. C. Teixeira and S. E. Belcher, On the structure of Langmuir turbulence, *Ocean Model.* **31**, 105 (2010).
- [13] S. E. Belcher, A. L. M. Grant, K. E. Hanley, B. Fox-Kemper, L. Van Roekel, P. P. Sullivan, W. G. Large, A. Brown, A. Hines, D. Calvert, A. Rutgersson, H. Pettersson, J.-R. Bidlot, P. A. E. M. Janssen, and J. A. Polton, A global perspective on Langmuir turbulence in the ocean surface boundary layer, *Geophys. Res. Lett.* **39**, L18605 (2012).
- [14] E. A. D'Asaro, J. Thomson, A. Y. Shcherbina, R. R. Harcourt, M. F. Cronin, M. A. Hemer, and B. Fox-Kemper, Quantifying upper ocean turbulence driven by surface waves, *Geophys. Res. Lett.* **41**, 102 (2014).
- [15] Q. Li, A. Webb, B. Fox-Kemper, A. Craig, G. Danabasoglu, W. G. Large, and M. Vertenstein, Langmuir mixing effects on global climate: WAVEWATCH III in CESM, *Ocean Model.* **103**, 145 (2016).
- [16] I. Langmuir, Surface motion of water induced by wind, *Science* **87**, 119 (1938).
- [17] S. Leibovich, The form and dynamics of langmuir circulations, *Annu. Rev. Fluid Mech.* **15**, 391 (1983).
- [18] S. Thorpe, Langmuir circulation, *Annu. Rev. Fluid Mech.* **36**, 55 (2004).
- [19] E. A. D'Asaro, Turbulent vertical kinetic energy in the ocean mixed layer, *J. Phys. Oceanogr.* **31**, 3530 (2001).
- [20] R.-S. Tseng and E. A. D'Asaro, Measurements of turbulent vertical kinetic energy in the ocean mixed layer from Lagrangian floats, *J. Phys. Oceanogr.* **34**, 1984 (2004).
- [21] J. A. Smith, Observations and theories of langmuir circulation: A story of mixing, in *Fluid Mechanics and the Environment: Dynamical Approaches* (Springer, Berlin, 2001), pp. 295–314.
- [22] A. Gargett, J. Wells, A. E. Tejada-Martínez, and C. E. Grosch, Langmuir supercells: A mechanism for sediment resuspension and transport in shallow seas, *Science* **306**, 1925 (2004).
- [23] Q. Li and B. Fox-Kemper, Assessing the effects of Langmuir turbulence on the entrainment buoyancy flux in the ocean surface boundary layer, *J. Phys. Oceanogr.* **47**, 2863 (2017).
- [24] R. A. Weller and J. F. Price, Langmuir circulation within the oceanic mixed layer, *Deep Sea Res. Part A. Oceanogr. Res. Pap.* **35**, 711 (1988).
- [25] S. A. Thorpe, T. R. Osborn, J. F. E. Jackson, A. J. Hall, and R. G. Lueck, Measurements of turbulence in the upper-ocean mixing layer using autosub, *J. Phys. Oceanogr.* **33**, 122 (2003).
- [26] P. P. Sullivan, J. C. McWilliams, and W. K. Melville, Surface gravity wave effects in the oceanic boundary layer: Large-eddy simulation with vortex force and stochastic breakers, *J. Fluid Mech.* **593**, 405 (2007).
- [27] A. L. M. Grant and S. E. Belcher, Characteristics of Langmuir turbulence in the ocean mixed layer, *J. Phys. Oceanogr.* **39**, 1871 (2009).
- [28] J. C. McWilliams, E. Huckle, J.-H. Liang, and P. P. Sullivan, Langmuir turbulence in swell, *J. Phys. Oceanogr.* **44**, 870 (2014).
- [29] A. Webb and B. Fox-Kemper, Wave spectral moments and Stokes drift estimation, *Ocean Model.* **40**, 273 (2011).
- [30] J. A. Polton and S. E. Belcher, Langmuir turbulence and deeply penetrating jets in an unstratified mixed layer, *J. Geophys. Res.: Oceans* **112**, 1 (2007).
- [31] M. Li and C. Garrett, Mixed layer deepening due to Langmuir circulation, *J. Phys. Oceanogr.* **27**, 121 (1997).
- [32] J. A. Smith, Evolution of Langmuir circulation during a storm, *J. Geophys. Res.: Oceans* **103**, 12649 (1998).
- [33] T. Kukulka, A. J. Plueddemann, J. H. Trowbridge, and P. P. Sullivan, Rapid mixed layer deepening by the combination of Langmuir and shear instabilities: A case study, *J. Phys. Oceanogr.* **40**, 2381 (2010).
- [34] B. G. Reichl, D. Wang, T. Hara, I. Ginis, and T. Kukulka, Langmuir turbulence parameterization in tropical cyclone conditions, *J. Phys. Oceanogr.* **46**, 863 (2016).

- [35] J. S. Turner, Turbulent entrainment: The development of the entrainment assumption, and its application to geophysical flows, *J. Fluid Mech.* **173**, 431 (1986).
- [36] A. E. Tejada-Martínez and C. E. Grosch, Langmuir turbulence in shallow water. Part 2. Large-eddy simulation, *J. Fluid Mech.* **576**, 63 (2007).
- [37] M. A. C. Teixeira and S. E. Belcher, On the distortion of turbulence by a progressive surface wave, *J. Fluid Mech.* **458**, 229 (2002).
- [38] M. A. C. Teixeira, A linear model for the structure of turbulence beneath surface water waves, *Ocean Model.* **36**, 149 (2011).
- [39] C.-H. Moeng, A large-eddy-simulation model for the study of planetary boundary-layer turbulence, *J. Atmos. Sci.* **41**, 2052 (1984).
- [40] J. Smagorinsky, General circulation experiments with the primitive equations I. The basic experiment, *Mon. Weather Rev.* **91**, 99 (1963).
- [41] J. W. Deardorff, Stratocumulus-capped mixed layers derived from a three-dimensional model, *Bound.-Layer Meteorol.* **18**, 495 (1980).
- [42] J. L. Lumley and G. R. Newman, The return to isotropy of homogeneous turbulence, *J. Fluid Mech.* **82**, 161 (1977).
- [43] J. L. Lumley, Computational modeling of turbulent flows, in *Advances in Applied Mechanics* (Elsevier, Amsterdam, 1979), Vol. 18, pp. 123–176.
- [44] K.-S. Choi and J. L. Lumley, The return to isotropy of homogeneous turbulence, *J. Fluid Mech.* **436**, 59 (2001).
- [45] S. Banerjee, R. Krahl, F. Durst, and C. Zenger, Presentation of anisotropy properties of turbulence, invariants versus eigenvalue approaches, *J. Turbul.* **8**, N32 (2007).
- [46] K. McCaffrey, B. Fox-Kemper, P. E. Hamlington, and J. Thomson, Characterization of turbulence anisotropy, coherence, and intermittency at a prospective tidal energy site: Observational data analysis, *Renew. Energy* **76**, 441 (2015).
- [47] L. Van Roekel, B. Fox-Kemper, P. Sullivan, P. Hamlington, and S. Haney, The form and orientation of langmuir cells for misaligned winds and waves, *J. Geophys. Res.: Oceans* **117**, C05001 (2012).
- [48] J. C. R. Hunt, A. A. Wray, and P. Moin, Eddies, stream, and convergence zones in turbulent flows, Center for Turbulence Research Report CTR-S88 (1988).
- [49] M. S. Chong, A. E. Perry, and B. J. Cantwell, A general classification of three-dimensional flow fields, *Phys. Fluids A* **2**, 765 (1990).
- [50] J. Soria, R. Sondergaard, B. J. Cantwell, M. S. Chong, and A. E. Perry, A study of the fine-scale motions of incompressible time-developing mixing layers, *Phys. Fluids* **6**, 871 (1994).
- [51] Y. Dubief and F. Delcayre, On coherent-vortex identification in turbulence, *J. Turbul.* **1**, N11 (2000).
- [52] A. Okubo, Horizontal dispersion of floatable particles in the vicinity of velocity singularities such as convergences, *Deep Sea Res. Oceanogr. Abstr.* **17**, 445 (1970).
- [53] J. Weiss, The dynamics of enstrophy transfer in two-dimensional hydrodynamics, *Phys. D* **48**, 273 (1991).
- [54] C. Pasquero, A. Provenzale, and J. B. Weiss, Vortex Statistics from Eulerian and Lagrangian Time Series, *Phys. Rev. Lett.* **89**, 284501 (2002).
- [55] J. Isern-Fontanet, J. Font, E. García-Ladona, M. Emelianov, C. Millot, and I. Taupier-Letage, Spatial structure of anticyclonic eddies in the algerian basin (mediterranean sea) analyzed using the okubo–weiss parameter, *Deep Sea Res. Part II: Top. Stud. Oceanogr.* **51**, 3009 (2004).
- [56] A. Lohrmann, R. Cabrera, G. Gelfenbaum, and J. Haines, Direct measurements of Reynolds stress with an acoustic Doppler velocimeter, in *Proceedings of the IEEE 5th Working Conference on Current Measurement*, St. Petersburg, FL, USA (IEEE, New York, 1995), pp. 205–210.
- [57] J. Thomson, B. Polagye, V. Durgesh, and M. C. Richmond, Measurements of turbulence at two tidal energy sites in Puget Sound, WA, *IEEE J. Ocean. Eng.* **37**, 363 (2012).
- [58] github.com/qingli411/anisotropic_barycentric_map.
- [59] B. G. Reichl and Q. Li, A parameterization with a constrained potential energy conversion rate of vertical mixing due to Langmuir turbulence, *J. Phys. Oceanogr.* **49**, 2935 (2019).

- [60] R. R. Harcourt, A second-moment closure model of Langmuir turbulence, *J. Phys. Oceanogr.* **43**, 673 (2013).
- [61] R. R. Harcourt, An improved second-moment closure model of Langmuir turbulence, *J. Phys. Oceanogr.* **45**, 84 (2015).
- [62] J. Rotta, Statistische Theorie nichthomogener Turbulenz, *Z. Phys.* **129**, 547 (1951).